Supplementary Material

X-ray detection of ultrashort spin current pulses in synthetic antiferromagnets

C. Stamm,[1,2,a)] C. Murer,[1] M. S. Wörnle,[1,3] Y. Acremann,[4] R. Gort,[4,5] S. Däster,[4] A. H. Reid,[6] D. J. Higley,[6,7,8] S. F. Wandel,[6] W. F. Schlotter,[6] and P. Gambardella[1]

[1)] *Department of Materials, ETH Zurich, 8093 Zurich, Switzerland*

[2)] *Institute for Electric Power Systems, University of Applied Sciences and Arts Northwestern Switzerland, 5210 Windisch, Switzerland*

[3)] *Department of Physics, ETH Zurich, 8093 Zurich, Switzerland*

[4)] *Laboratory for Solid State Physics, ETH Zurich, 8093 Zurich, Switzerland*

[5)] *European XFEL GmbH, Holzkoppel 4, 22869 Schenefeld, Germany*

[6)] *Linac Coherent Light Source, SLAC National Accelerator Laboratory, 2575 Sand Hill Road, Menlo Park, CA 94025, USA*

[7)] *Stanford Institute for Materials and Energy Sciences, SLAC National Accelerator Laboratory, 2575 Sand Hill Road, Menlo Park, CA 94025, USA*

[8)] *Department of Applied Physics, Stanford University, Stanford, CA 94305, USA*

[a)] christian.stamm@fhnw.ch

SM 1. SIGNAL CORRELATION AND DETECTOR LINEARITY

In order to measure the x-ray absorption, we recorded the transmitted x-ray intensity on a CCD detector by integration over all pixels, on a shot to shot basis with 120 Hz repetition rate. These values are divided by the incoming intensity, which is measured using two different methods. A fluorescence intensity monitor, operated in its MCP mode, detected both fluorescence and electrons from an x-ray mirror[S1]. In addition, an MCP detector looking at the fluorescence from a Silicon membrane was used. Detector linearity is ensured by plotting the correlation of the two measured signals in Fig. S1. For the normalization of our measurements, we selected the detector at the Silicon membrane, as it had a higher correlation with the transmitted signal.

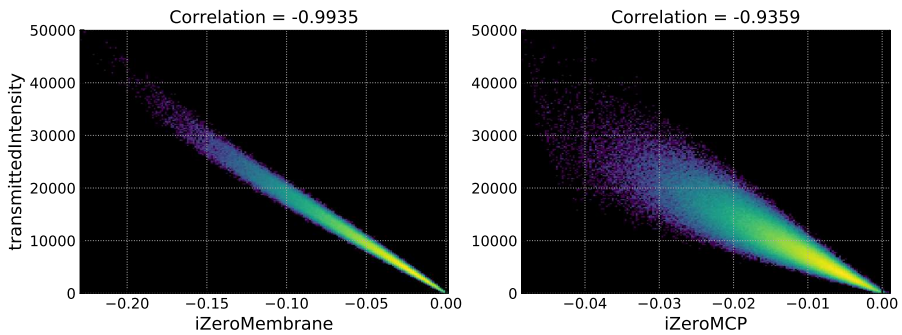

FIG. S1. Correlation of the transmitted intensity measured on a CCD, with the incoming intensity recorded either at a Si membrane placed in the x-ray beam, or on a MCP that detects fluorescence and secondary electrons from an x-ray mirror.

SM 2. PUMP PROBE TIMING: 60 Hz JITTER CORRECTION

Even with x-ray and laser pulses of sub-100 fs duration, the time resolution of a laser pump – x-ray probe experiment may be worse due to arrival time jitter of the individual pulses. A known fact is that the LCLS electron bunch, and with it the generated x-ray pulse, has a timing jitter alternating with 60 Hz, for 120 Hz pulse repetition. Several options for handling the timing jitter have been tested in the data analysis, and we selected the second one for the presented graphs for stability reasons, and confirmed its credibility by comparison with the third option.

- Use original data without any time jitter correction: useful for quick online visualization of results. Depending on the jitter amplitude, XMCD decay times may increase to > 500 fs.
- Divide measurements into two 60 Hz bins, in order to separate the two alternating states with different x-ray arrival times. After that, perform individual fits of the XMCD data. For each bin, subtract their time-zero before combining to a common data set.
- Apply same division of the data as above. Use the phase cavity information that monitors the electron bunch arrival (see Fig. S2) to obtain the average time shift between the 60 Hz bins, then shift time-zero of one bin accordingly before combining to a common data set. This procedure gives similar results as the XMCD fitting method above, and does not need a measured dynamic signal from the sample.
- Use phase cavity data for shot-to-shot based correction. This procedure may have more noise, depending on data quality. Also long-term drifts of e.g. the pump laser line are not accounted for (see next two points for their inclusion).
- Apply a custom sorting algorithm based on the best correlation in the phase cavity corrected data from above, after averaging a few minutes of data[S2] outlined in[S3], improved in[S4] and combined with a maximum-likelihood estimation[S5]. If strong time-dependent changes are absent from the data, this method cannot be applied.

- Use time tool data, filtered by 100-1000 events to extract long-term drifts from the high noise level present in the timing data while operating with the delta undulator. For shot-to-shot correction, the phase cavity data is used. While this procedure has the best potential for precise jitter correction, unfortunately only very few data sets recorded with the circular polarization from the delta undulator have valid time tool data, due to the one order of magnitude lower x-ray intensity.

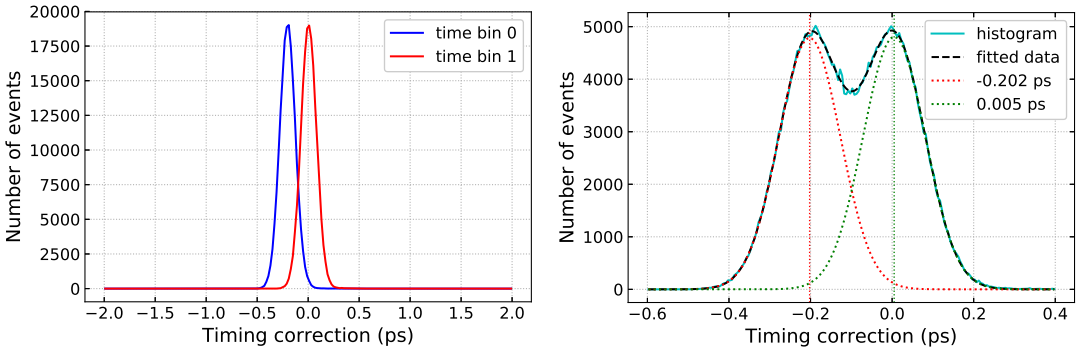

FIG. S2. Phase cavity diagnostic of the arrival time correction. Left: histogram of the phase cavity arrival time correction, separated into two bins according to odd/even pulse number. Right: fitting a double Gaussian pulse reveals the time shift between the bins to be 0.207 ps.

SM 3. ADDITIONAL TIME SCANS ON Ni/Ru/Fe

XMCD time scans on the Ni/Ru/Fe sample with parallel alignment of the Ni and Fe magentization are plotted in Fig. S3, layer resolved to display the (upper) Ni and (lower) Fe layer.

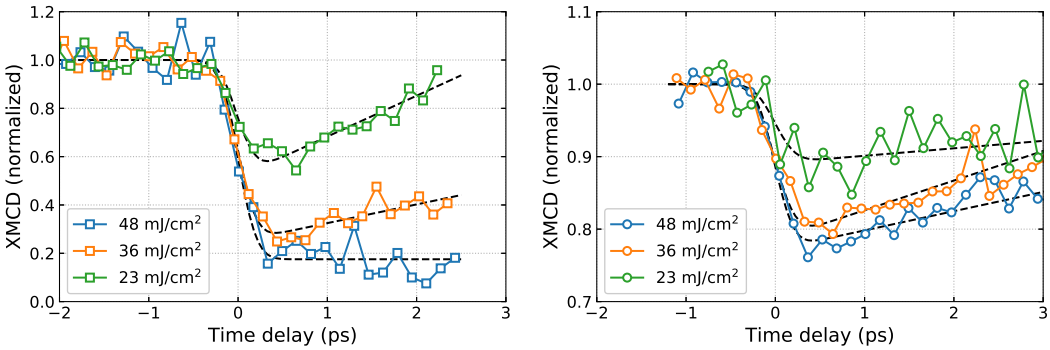

FIG. S3. XMCD time scans on Ni/Ru/Fe with photon energy set to the Ni L_3 (left) and Fe L_3 (right) edges, for indicated pump laser fluences. The magnetic layers were oriented parallel through a magnetic field.

SM 4. ADDITIONAL SPECTRA ON Ni/Ru/Fe

Besides time-scans recorded at fixed photon energy, we recorded XAS spectra around the L_3 absorption edges, applying four different magnetic fields. This forced the magnetization directions of the Ni and Fe layers into each of the four possible configurations, with two parallel and two antiparallel configurations. From these spectra, we calculate the dichroism for parallel and antiparallel configuration. In order to obtain a common normalization of the two XMCD spectra, we also recorded for each spectrum the sample in equilibrium, e.g. without pump laser pulse. The measurements for four different pump laser fluences are plotted in Fig. S4.

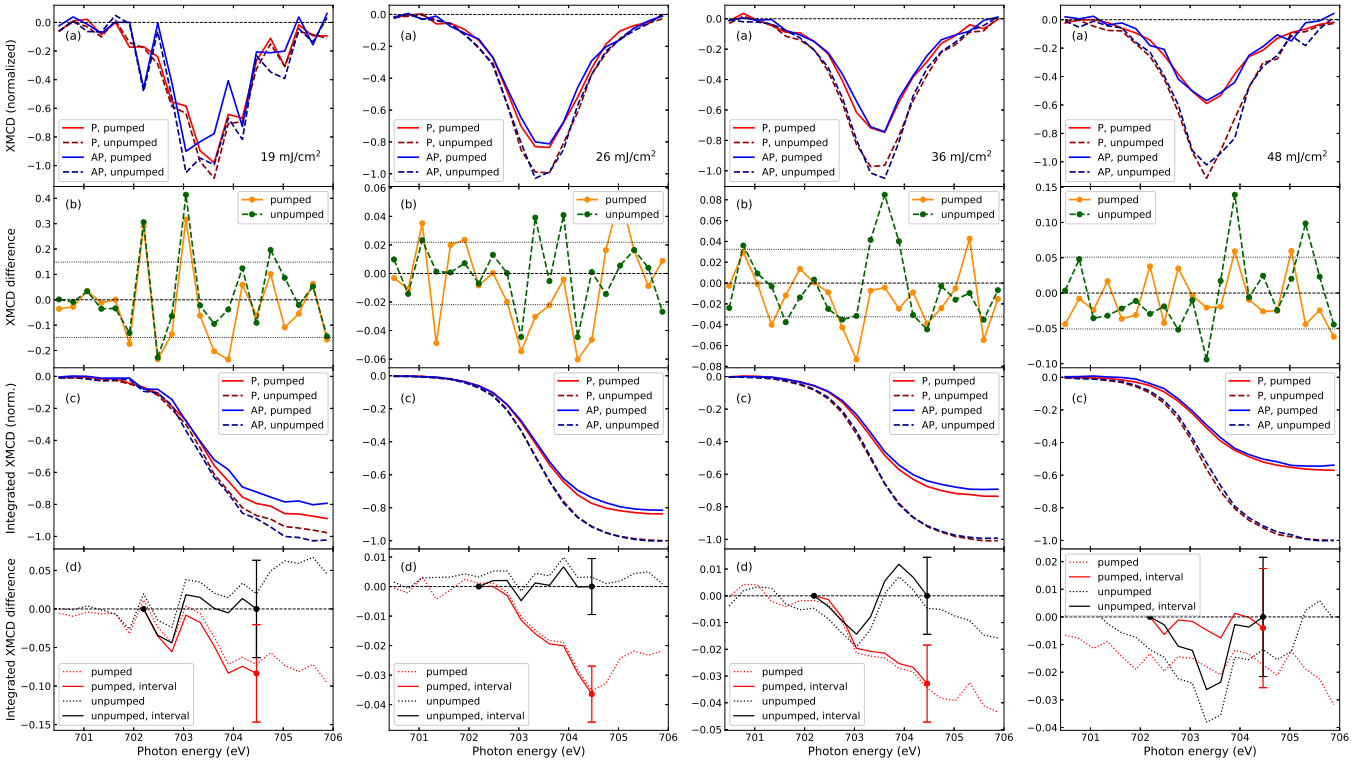

FIG. S4. Ni/Ru/Fe XMCD measured at ≈1 ps after excitation. Four measurements with increasing pump fluence are shown, as indicated in the top panels. (a) XMCD of both relative magnetization orientations, parallel (P) and antiparallel (AP), for the pumped and unpumped sample. (b) XMCD difference of P and AP, (c) integration of the XMCD curves shown in (a), normalized to the value of the unpumped sample. (d) difference of the integrated XMCD. Note the large XMCD fluctuations in the 19 mJ/cm^2 panel, causing a poor match of the unpumped curves in (c) and increased error margins in (d) for this fluence.

SM 5. fs LASER INDUCED CHANGE IN XAS

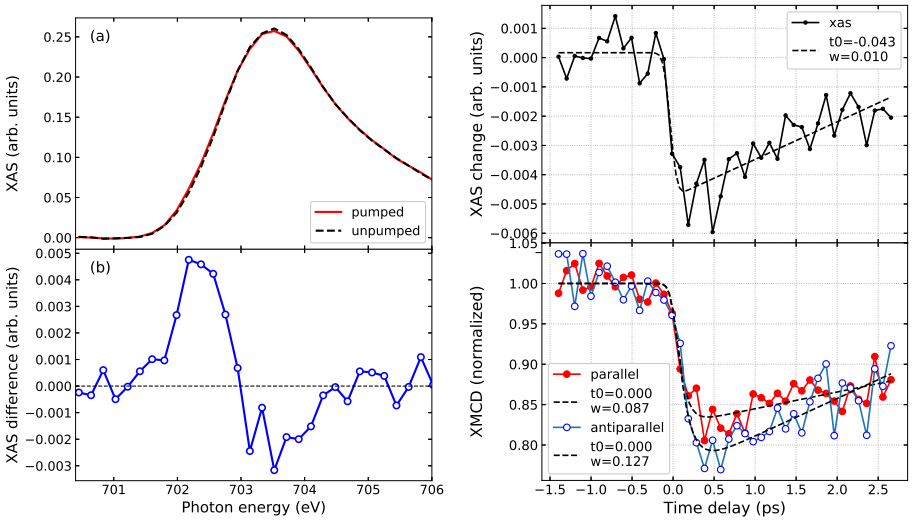

FIG. S5. Left: Ni/Ru/Fe XAS spectra at the Fe L_3 absorption edge: (a) laser pumped and unpumped absorption and (b) their difference. Right: Ni/Ru/Fe time dependent XAS changes and XMCD for parallel and antiparallel magnetization orientation, all measured at the Fe L_3 absorption edge, with 26 mJ/cm^2 pumping fluence.

Besides the obvious time resolved changes in the XMCD signals as presented in the main text, we observed subtle changes in the absorption lines, which may be seen as footprint of the laser excited electronic system. Similar as in previous fs XAS measurements on $3d$ transition metals[S6,S7], a slight shift of the absorption line towards lower photon energies can be seen in Fig. S5(left). The dynamic response of the XAS change directly relates to the XMCD dynamics as shown on the right in Fig. S5. These data were corrected for their timing jitter using the time tool data (last option in SM 2), resulting in an improved time resolution at cost of a slightly increased intensity noise.

SM 6. ADDITIONAL DATA ON Ni/Cu/Fe

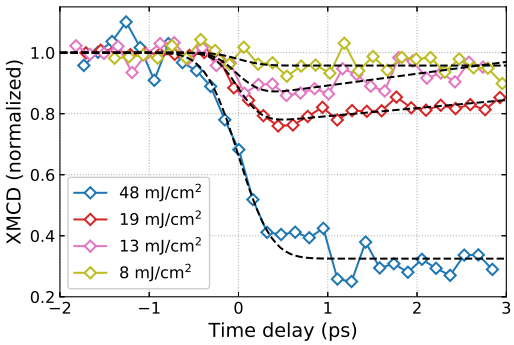

FIG. S6. Ni/Cu/Fe XMCD at the Fe L_3 absorption edge as function of pump-probe time delay, excited with the indicated pump laser fluence.

Time resolved XMCD data on the Ni(5 nm)/Cu(30nm)/Fe(4 nm) is presented in Fig. S6, for different pump laser fluences. The Ni and Fe magnetization directions were always aligned parallel. XMCD spectra of the laser pumped and unpumped sample are plotted in Fig. S7 for increasing pump laser fluences.

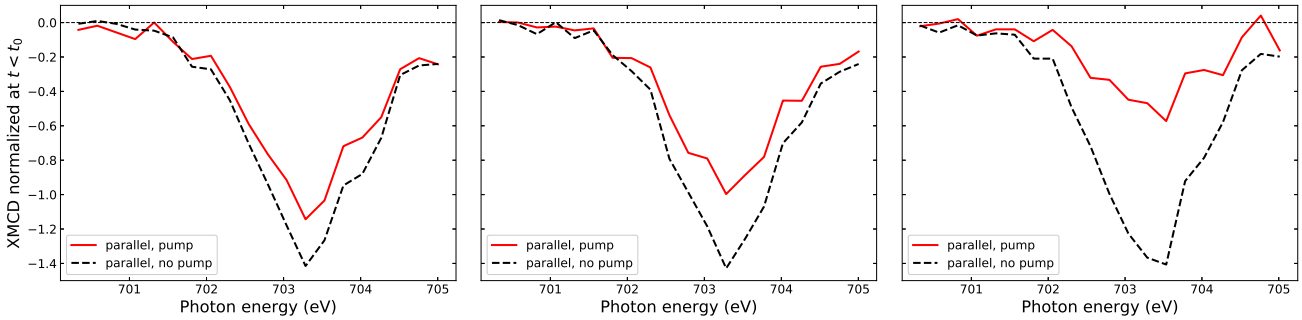

FIG. S7. Ni/Cu/Fe XMCD at the Fe L_3 absorption edge, excited with the indicated pump laser fluence, (below) spectra measured at fixed time delay of ≈1 ps and at increasing fluences of 19, 26, and 48 mJ/cm^2 (left to right).

SM 7. MODELING OF THE LASER ABSORPTION IN MULTILAYER SAMPLES

The absorption of the exciting laser pulse is modeled within a transfer matrix calculation[S8], in order to obtain the absorbed energy in each layer. Fig. S8 shows the resulting Poynting vector S, the differential absorption $dA(z)$ and the depth-dependent absorption $A(z)$. The results are summarized in Table S1. It becomes apparent, that for Ni/Ru/Fe the Fe layer is still affected by the pump laser beam, although not as strong as the Ni layer. In Ni/Cu/Fe, the absorption in Fe may be neglected. Both samples have a very strong overall reflectivity, which is due to the Al deposition on the back of the Si_3N_4 membrane. Especially the absorption in the magnetic layers in the Ni/Ru/Fe

sample is strongly reduced. This is the reason for the rather high incident fluence for the laser excitation applied during the measurements. As a comparison, the last column in Table S1 states calculated values for a Ni/Ru/Fe sample that would have no Al layer on the back of the Si_3N_4 membrane. While the absorption in the magnetic layers is much stronger, the ratio $A(\mathrm{Ni})/A(\mathrm{Fe})$ is almost the same as for the measured sample with heat sink. Adjusting the incident pump laser fluence to account for the sample reflectivity, we thus get comparable excitation profiles across the Ni/Ru/Fe stack, with and without Al back coating.

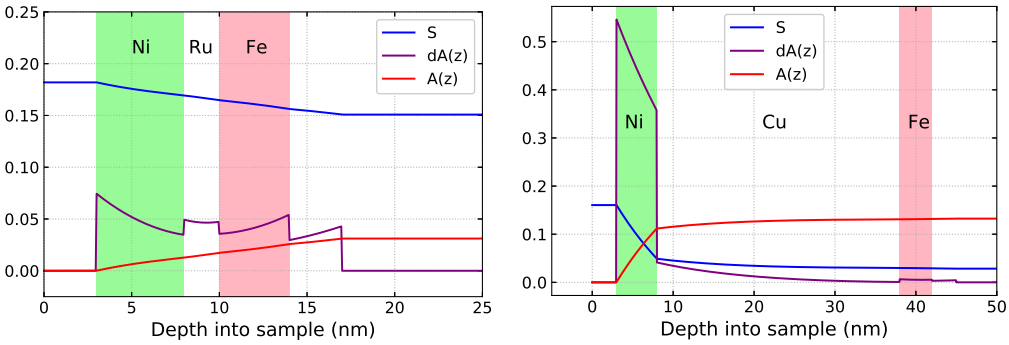

FIG. S8. Simulated optical absorption in multilayered samples. Left, $AlO_x(3)/Ni(5)/Ru(2)/Fe(4)/Ta(3)/Si_3N_4(188)/Al(100)$ and right, $AlO_x(3)/Ni(5)/Cu(30)/Fe(4)/Ta(3)/Si_3N_4(188)/Al(100)$, with layer thickness in nm stated in parentheses.

Quantity		Ni/Ru/Fe	Ni/Cu/Fe	Ni/Ru/Fe (no Al)
Sample absorption	A	0.1818	0.1608	0.4682
Absorption in Ni	$A(\mathrm{Ni})$	0.0125	0.1112	0.1860
Absorption in Fe	$A(\mathrm{Fe})$	0.0085	0.0011	0.1220
Absorption ratio	$A(\mathrm{Ni})/A(\mathrm{Fe})$	1.47	101.3	1.52
Reflected intensity	R	0.818	0.839	0.2563

TABLE S1. Simulated absorption of the pump pulse in the Ni and Fe layers. Last column: ficticious sample without Al layer.

REFERENCES

[S1]P. Heimann, A. Reid, Y. Feng, and D. Fritz, "Fluorescence intensity monitors as intensity and beam-position diagnostics for x-ray free-electron lasers," J. Synchrotron Rad. **26**, 358–362 (2019).

[S2]L. LeGuyader, private communication (2018).

[S3]C. D. Woody, "Characterization of an adaptive filter for the analysis of variable latency neuroelectric signals," Medical & Biological Engineering **5**, 539–554 (1967).

[S4]A. Cabasson and O. Meste, "Time delay estimation: A new insight into the Woody's method," IEEE Signal Processing Letters **15**, 573–576 (2008).

[S5]K. Kim, S.-H. Lim, J. Lee, W.-S. Kang, C. Moon, and J.-W. Choi, "Joint maximum likelihood time delay estimation of unknown event-related potential signals for EEG sensor signal quality enhancement," Sensors **16** (2016), 10.3390/s16060891.

[S6]C. Stamm, T. Kachel, N. Pontius, R. Mitzner, T. Quast, K. Holldack, S. Khan, C. Lupulescu, E. F. Aziz, M. Wietstruk, H. A. Dürr, and W. Eberhardt, "Femtosecond modification of electron localization and transfer of angular momentum in nickel," Nat. Mater. **6**, 740 (2007).

[S7]C. Boeglin, E. Beaurepaire, V. Halté, V. López-Flores, C. Stamm, N. Pontius, H. A. Dürr, and J.-Y. Bigot, "Distinguishing the ultrafast dynamics of spin and orbital moments in solids," Nature **465**, 458–461 (2010).

[S8]S. J. Byrnes, "Multilayer optical calculations," (2016), arXiv:1603.02720.